Key Engineering Materials
ISSN: 1662-9795, Vol. 926, pp 1399-1412
doi:10.4028/p-cr2tco

Submitted: 2021-12-17
Revised: 2022-01-24
Accepted: 2022-02-18
Online: 2022-07-22

Towards 3D Process Simulation for In-Situ Hybridization of Fiber-Metal-Laminates (FML)

Christian T. Poppe[1,5,a*], Henrik O. Werner[1,2,b], Moritz Kruse[3,c], Hui Chen[3,d], Noomane Ben Khalifa[3,e], Frank Henning[1,4,f], and Luise Kärger[1,g]

[1]Karlsruhe Institute of Technology (KIT), Institute for Vehicle System Technology (FAST), Division Lightweight Technology, Germany

[2]Karlsruhe Institute of Technology (KIT), Institute for Applied Materials (IAM), Germany

[3]Leuphana University Lüneburg (LUL), Institute of Product and Process Innovation (PPI), Germany

[4]Fraunhofer Institute for Chemical Technology (ICT), Polymer Engineering Department, Germany

[5]Simutence GmbH, Germany

[a]christian.poppe@kit.edu, [b]henrik.werner@kit.edu, [c]moritz.kruse@leuphana.de, [d]hui.chen@leuphana.de, [e]noomane.benkhalifa@leuphana.de, [f]frank.henning@ict.fraunhofer.de, [g]luise.kaerger@kit.edu

Keywords: Composites, Hybrids, FSI, FE-Forming Simulation, FML, HY-LCM, RTM, Deep Drawing

Abstract. Fiber-metal-laminates (FML) provide excellent fatigue behavior, damage tolerant properties, and inherent corrosion resistance. To speed up manufacturing and simultaneously increase the geometrical complexity of the produced FML parts, Mennecart et al. [1] proposed a new single-step process combining deep-drawing with infiltration (HY-LCM). Although the first experimental results are promising, the process involves several challenges, mainly originating from the Fluid-Structure-Interaction (FSI) between deep-drawing and infiltration. This work aims to investigate those challenges to comprehend the underlying mechanisms. A new close-to-process test setup is proposed on the experimental side, combining deep-drawing of a hybrid stack with a linear infiltration. A process simulation model for FMLs is presented on the numerical side, enabling a prediction of the dry molding forces, local Fiber Volume Content (FVC) within the three glass fiber (GF) interlayers, and simultaneous fluid progression. The numerical results show that the local deformation of the hybrid stack and required forces are predictable. Furthermore, lateral sealing of the hybrid stacks leads to deviations from the intended initially one-dimensional fluid progression. Eventually, the numerical results demonstrate that most flow resistance originates from geometrically critical locations. Future experimental and numerical work will combine these insights to focus on the flow evaluation during deformation and a successful part-level application.

Introduction

In recent decades, the aerospace industry substantially drove Fiber Metal Laminate (FML) development and processing [2]. Combining the best features of metals and composite materials, FML provide excellent fatigue behavior, damage tolerant properties, inherent resistance to corrosion as well as good fire resistance [3, 4]. Products made of GLARE (Glass-Fiber Reinforced Aluminum Laminates) or ARALL (Aramid-Reinforced Aluminum Laminates) are usually produced in the autoclave chamber to achieve three-dimensional shapes [1]. However, using an autoclave chamber invokes a significant amount of manual work and an extra deep drawing tool for the metal layers. A new manufacturing process for double-curved components combining deep drawing with thermoplastic resin transfer molding (HY-LCM) in a single process step has been proposed by Mennecart et al. [1, 5].

A schematic illustration of the principal process steps is given in Fig 1. The stack is positioned between a matching punch and a die for processing. At the same time, the stack is clamped using circumferential blank holders. In the first step, the stack is only slightly deformed (5 to $10\,\mathrm{mm}$), which temporarily seals the outer rim. Subsequently, reactive resin is centrally injected through a hole in

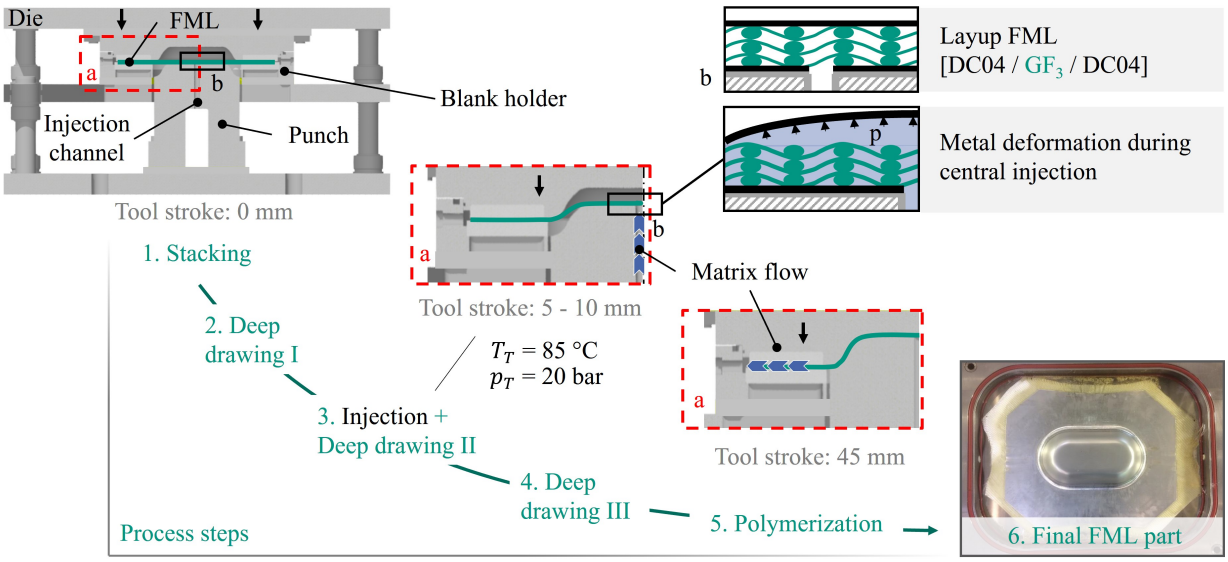

Fig. 1: Visualization of the combined deep-drawing and LCM process (HY-LCM) from Stacking (1.) to final polymerized part (6.) (adapted from [6]).

the lower metal layer while deep drawing proceeds. The fluid pressure can lead to slight buckling of the metal top layer during injection, as illustrated in Fig. 1. During the last $20\,\%$ of the tool stroke, the resin is forced outward and infiltrates the core GF layers. The heated molds enforce isothermal curing. Experiments show that this process design involves a variety of interrelated physical mechanisms, which need to be understood and utilized correctly to produce defect-free FML parts. Fluid-Structure-Interaction (FSI) between the deep drawing of the sheets, draping of the textile interlayers and infiltration provides severe challenges during processing. These interactions lead to dry spots, yarn fracture, buckling of the metal sheet, or local thickness variations [1, 5, 7]. In this regard, the interaction between the local deformation of the hybrid stack and infiltration is being investigated by a new close-to-process setup at LUL. The new device allows combining a deep drawing process with permeability measurements (cf. Fig. 2). Hence, infiltration trials close to processing conditions and investigation of reaction forces for different infiltration states becomes possible. Moreover, the experiments provide valuable data for developing and validating process simulation models at the KIT-FAST, supporting forthcoming virtual processes and part designs.

Aim and outline. This work presents a new device for close-to-process investigations of in-situ hybridization of FML. First results are used to develop and verify a process simulation model, which analyzes resulting deformation and infiltration conditions during testing. The main focus lies in modeling and demonstrating the coupled draping behavior of the hybrid stack, as this directly affects the local Fiber Volume Content (FVC) and thus infiltration. First, selected experimental results are presented. The process simulation model is presented and verified in the second step. Finally, the key insights are summarized.

Close-to-Process Trials

The experimental setup at the LUL combines a segmented deep-drawing tool for the hybrid stack with a one-directional flow measurement using a constant injection flow from right to left (cf. Fig. 2 (b)). A silicone oil with constant viscosity of $100\,\mathrm{mPas}$ is used for the trials. This value matches the initial viscosity of the thermoplastic matrix system in process trials. Hence, curing can be neglected during modeling. The FML in this study comprises two DC04 metal sheets (thickness $0.3\,\mathrm{mm}$) and three core layers of a glass twill fabric made ($280\,\mathrm{g/m^2}$, Interglas 92125 FK800).

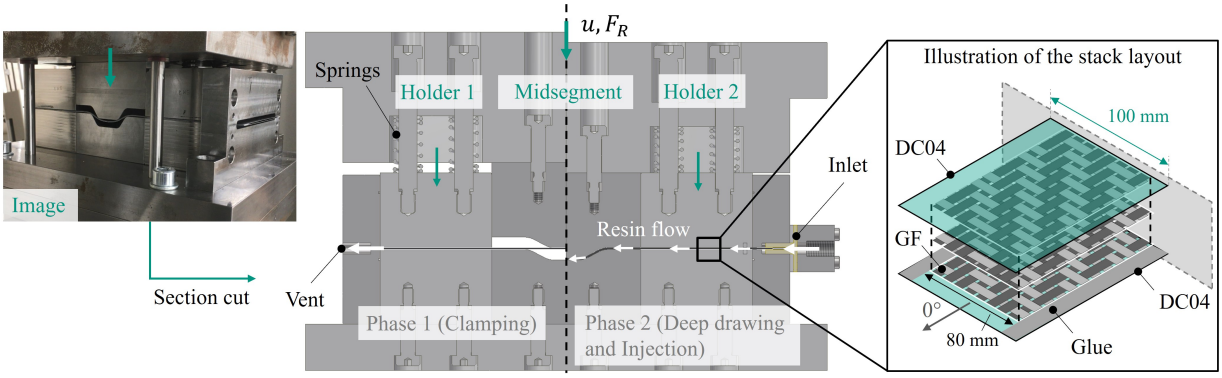

Fig. 2: Experimental setup | (a) Image during deep drawing of a hybrid stack; (b) Section cut of the segmented tool; (c) Illustration of the stack.

The device is placed inside a universal testing machine (Zwick/Roell Z250), which allows measuring reaction forces and prescribing closing profiles. Before testing, the hybrid stack is prepared to combine two DC04 (steel) cover layers and three glass fiber (GF) interlayers. Both lateral sides of the stack are glued under load by an adhesive sealant (Soudal Fix All Flexi) based on an SMX hybrid polymer to enforce a one-dimensional flow. Hence, the glue thickness matches the deformed GF stack height ($0.5\,\mathrm{mm}$). Deep-drawing trials proved no significant impact of the compliant sealing on the measured reaction forces. The GF layers width ($80\,\mathrm{mm}$) is reduced compared to the metal layers ($100\,\mathrm{mm}$). Hence, the resulting flow channel width is assumed to be $80\,\mathrm{mm}$. The length of the GF layers is $220\,\mathrm{mm}$, and that of the metal sheets is $245\,\mathrm{mm}$.

A test procedure comprises two phases. In the first phase (cf. Fig. 2 (b)), the stack is clamped on both sides via holder segments. Springs apply a final load of $456\,\mathrm{N}$ on each of the holder segments. The midsegment does not contact the stack in this first phase. Afterward, the midsegment deep draws the stack to a predefined position. The injection is started with a constant pressure of $5\,\mathrm{bar}$, while the tool position is caped constant. Hence, infiltration and deformation conditions can be investigated under close-to-process conditions, illustrated in Figure 1. Infiltration and deep-drawing can also be conducted simultaneously.

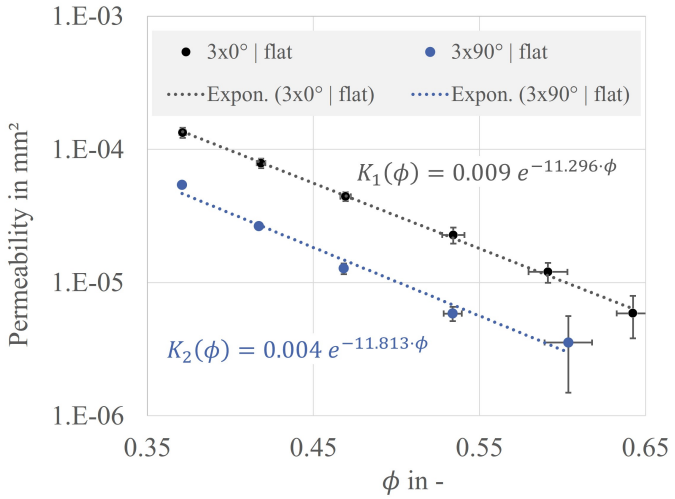

Fig. 3: In-plane permeability results obtained with a flat midsegment.

Permeability measurements. In addition to the deep drawing trials, the presented test setup is also used to measure the in-plane permeability components $K_1(\phi)$ and $K_2(\phi)$ of the GF textile for different FVCs (ϕ). Given that the fabric is not entirely balanced (cf. Fig. 2 (c)), both fiber orientations are investigated. A flat midsegment is used, and the two holders are fastened to the upper tool carrier

without springs. A one-dimensional Darcy flow with constant injection pressure ($5\,\mathrm{bar}$) is assumed to calculate the fully-saturated permeability. A constant viscosity of $100\,\mathrm{mPas}$ is used. This procedure is widely applied in the literature to determine the permeability of a porous media [8, 9]. The results for different FVCs are presented in Fig. 3.

Each trial is conducted three times with three GF layers. Results show an increased permeability in $0°$ direction compared to the $90°$ direction. The results are formalized using linear regression. The obtained functions for $K_1(\phi)$ and $K_2(\phi)$ are used for modeling fluid progression in the simulation.

Macroscopic Process Modeling

Literature review. The applied approach combines concepts from macroscopic draping simulations and mold filling fields. Finite-Element (FE)-based *macroscopic draping simulation* for continuous fiber-reinforced polymers (CoFRP) utilizes energy-related constitutive equations to describe deformation mechanisms of engineering fabrics. This approach allows predicting manufacturing defects and enables virtual feasibility studies before investing in costly equipment. Relevant processes in this context are preforming in advance to Resin Transfer Molding (RTM) [10], Wet Compression Molding (WCM) [11] and Thermoforming of unidirectional tapes or organosheets. Consequently, several simulation approaches and industrially applicable codes have been published in recent years, among many others by Willems [12], Haanappel [13] Boisse et al. [14, 15] and Dörr [16, 17], Comprehensive reviews have been provided by Boisse et al. [18] and Bussetta and Correia [19].

The second related field is *modeling of mold-filling and injection* in Liquid Compression Molding (LCM) of CoFRPs. Here, research mostly focuses on two industrial processes – Vacuum-Assisted-Resin-Injection (VARI) and RTM [20]. These simulation approaches aim to predict the mold filling behavior of large structures, especially under consideration of anisotropic permeability [21,22], curing of reactive resin systems [23,24] and Fluid-Structure-Interaction (FSI) [25,26]. Different modeling and solving techniques have been proposed in the literature, including Finite Volume (FV) [27] to Finite Differences (FD) [28] techniques. Moreover, conforming [29, 30] and non-conforming [31] FE-based formulations with additional control volumes (FE/CV) [22, 32] to account for mass conservation and interface flows are adopted.

Own approach. The applied *process model* in this contribution originates from WCM [11, 33, 34] and combines two fully-coupled submodels to describe the intra-ply behavior as illustrated in Fig. 4. An FE-based draping submodel captures the macroscopic deformation mechanism, such as membrane, bending, or compaction behavior. In contrast, the superimposed FE/CV-based fluid submodel supplies the fluid progression and pressure field by utilizing Darcy's law for porous media flow [11, 34, 35]. Both submodels are formulated in a three-dimensional manner, which enables a local prediction of fiber orientation and FVC, as well as modeling of squeeze-flow and infiltration in the thickness direction. This approach is used to model each textile layer of a fiber stack (intra-ply modeling).

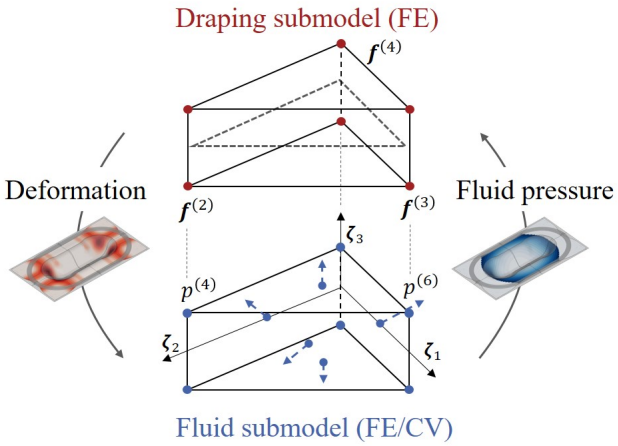

Fig. 4: Modeling approach at KIT combining two submodels to describe the intra-ply behavior of CoFRPs during processing [11].

To enable a simulation of the above introduced FML stack (cf. Fig. 2), the existing model needs to be adapted to the applied GF layers. Moreover, the metal sheets need to be added to the simulation because they strongly affect the local FVC. A numerical study without fluid progression and sufficient

compaction modeling has been carried out by Werner et al. [6] and proved the general feasibility of the approach taken.

Modeling of metal sheets. The DC04 metal sheets are modeled with conventional shell elements (S3) using an elastic-plastic material behavior with isotropic hardening. The latter is implemented using the Johnson-Cook material model in ABAQUS. The constant thickness of $0.3\,\mathrm{mm}$ is prescribed to the section. The material parameters are summarized in Tab. 1 and originate from experiments and numerical studies carried out by Trzepiecinski and Lemu [36] for the same material. A rate- and temperature dependency is neglected.

Table 1: Material parameters for metal sheet modeling.

Elastic	E_{DC04} (N/mm^2)	Poissons's ratio	κ_{11} in N/mm^2	κ_{22} in N/mm^2
	210000	0.3	59817.3	59817.3
Plastic	A in N/mm^2	B in N/mm^2	Flow-curve expo. n	T-dependency m
Johnson-Cook	191.02	558.57	0.208	0

Modeling of GF layers. Following the above-introduced duality of the modeling approach, deformation behavior and permeability require adaptation to the GF material. In the context of this study, the deformation of the GF plies is dominated by compaction, as the single-curved tool geometry does not require an in-plane shearing of the textile layers. Given the quasi inextensibility of the fibers in $0\,^\circ$ direction, a purely elastic material model is sufficient ($E_{\mathrm{f1}} = E_{\mathrm{f2}} = 1000\,\mathrm{N/mm^2}$). Similarly, the transverse shear stiffnesses of the metal sheets are several decades above the values for the textile layers ($\kappa_{\mathrm{GF},11}, \kappa_{\mathrm{GF},22} = 0.03$ N/mm^2). Hence, the contributed bending stiffness of GF layers is negligibly low. This circumstance is beneficial, as the applied draping submodel utilizes a reduced-integrated continuum shell element in ABAQUS (SC6R), which cannot account for a decoupled description of membrane and bending behavior – usually required for CoFRPs [15].

Modeling of the *compaction behavior* is not implemented within the SC element but in the superimposed user-element using a hyper-elastic material formulation (St. Venant-Kirchhoff material). This approach is required, as only a non-linear compaction modulus E_3 can sufficiently describe the material behavior [34,37,38]. For modeling, only the 3-component addressing the thickness direction in the stiffness matrix is non-zero:

$$E_3 = E_3^{\mathrm{Mat}}(\varepsilon_3^{\mathrm{GL}}) + E_3^{\mathrm{Lock}} \quad \text{with} \quad E_3^{\mathrm{Mat}}(\varepsilon_3^{\mathrm{GL}}) = a_0 e^{[\varepsilon_{\mathrm{I}}(\varepsilon_3^{\mathrm{GL}} - \varepsilon_{\mathrm{II}})] + \varepsilon_{\mathrm{III}}} \quad \text{of} \quad \varepsilon_3^{\mathrm{GL}} > \varepsilon_{3,\mathrm{s}}^{\mathrm{GL}}\,. \tag{1}$$

Eq. 1 contains a parametrized non-linear material part E_3^{Mat}, which utilizes the material parameters $a_0, \varepsilon_{\text{I-III}}$. Moreover, Eq. 1 comprises additional non-physical smooth locking part E_3^{Lock}, that only contributes for compaction states outside the experimentally acquired data range as described in [34]. This prevents collapsing for temporarily high compressed elements during draping. E_3^{Mat} itself is formulated based on the current Green-strain in thickness direction $\varepsilon_3^{\mathrm{GL}}$. The nodal reaction force matrix $\hat{\boldsymbol{f}}_{\mathrm{R}}^{\mathrm{mat}}$ of the iso-parametric wedge element with respect to ABAQUS' Green-Naghdi's frame are determined by

$$\hat{\boldsymbol{f}}_{\mathrm{R}}^{\mathrm{mat}} = \frac{1}{J} \cdot \det(\boldsymbol{J}) \cdot \boldsymbol{B}\,\tilde{\boldsymbol{\tau}} \quad \text{with} \quad \tilde{\boldsymbol{\tau}} = \tilde{\boldsymbol{F}} \cdot \boldsymbol{C} \cdot \tilde{\boldsymbol{E}}\,. \tag{2}$$

Here, the Kirchhoff stress vector $\tilde{\boldsymbol{\tau}}$ (Voigt notation) is calculated by means of deformation gradient $\tilde{\boldsymbol{F}}$, Green-Lagrange strain $\tilde{\boldsymbol{E}}$ and the above introduced stiffness matrix $\boldsymbol{C}$. In Eq. 2, $\boldsymbol{B}$ is the operator matrix containing the derivatives of the element shape functions and J the Jacobean matrix.

Compaction trials are used to identify the material parameters via reverse identification. The initial thickness of the material is assumed to be $0.4\,\mathrm{mm}$. Final thickness ranges around $0.17\,\mathrm{mm}$ for a FVC of $65\,\%$. As outlined in Fig. 5, a good agreement between experimental data and simulation model is

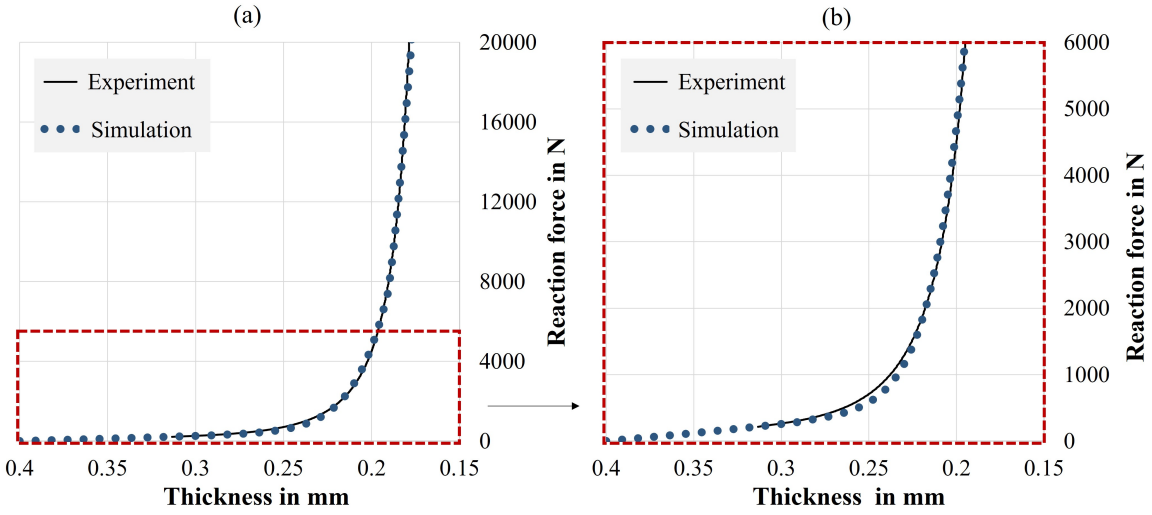

Fig. 5: (a) Comparison of measured and predicted reaction forces during compaction for an area of $200\,\mathrm{mm}$ x $100\,\mathrm{mm}$; (b) Close-up on lower compression states.

achieved. Compaction trials were only conducted once. Hence, no standard deviation can be presented. The model must predict the initially low compaction stiffness during the first phase of compaction and the stiffness transition towards material locking for FVC above $65\,\%$. The material parameters are summarized in Tab. 2.

Table 2: Material parameters for compaction modeling of the GF layers.

E_{SC} in N/mm^2	$\varepsilon_{3,\mathrm{s}}^{\mathrm{GL}}$ in -	a_0 in N/mm^2	ε_{I} in -	$\varepsilon_{\mathrm{II}}$ in -	$\varepsilon_{\mathrm{III}}$ in -
0.046	0.25	1.0	45.95	0.573	0.2

Modeling of tooling and interfaces. The tool is discretized using rigid surfaces and individual instances for the four tool segments. Closing of the midsegment (cf. Fig. 2 (b)) is implemented using a displacement boundary condition. The loads for both holders originating from the springs are directly prescribed using load boundary condition, which considers the current midsegments position.

Contact behavior at ply and tool interfaces is modelled using a penalty-based contact algorithms in ABAQUS/explicit. To prevent excessive contact penetration, a contact normal stiffness of $200\,\mathrm{N/mm^2}$ is required, combined with a contact damping of $1\,\mathrm{N/mms}$. Different friction coefficients are used to contribute to the three contact pairs ($\mu_{\text{Tool-Metal}} = 0.2$, $\mu_{\text{Metal-Ply}} = 0.253$, $\mu_{\text{Ply-Ply}} = 0.334$).

Modeling of infiltration. Richard's law [21] combining mass conservation and Darcy's law is applied in a transient explicit formulation (cf. Eq. 3) [34] and is embedded in the superimposed user element (cf. Fig. 4), to solve the pressure field and model flow front progression:

$$\int_{V_\mathrm{k}} \rho C_{\mathrm{hyd}}\, \dot{p}\, \mathrm{d}v = \frac{\boldsymbol{K}(\phi)}{\eta\, \varphi} \int_{V_\mathrm{k}} \mathrm{div}\left(\mathrm{grad}\,(p) - \rho \boldsymbol{g}\right)\, \mathrm{d}v\,. \tag{3}$$

This approach allows modeling a transient single-phase fluid progression that only implicitly accounts for the velocity field. A hydraulic capacity C_{hyd} is introduced to enable an explicit time integration. The above determined in-plane permeability functions $K_1(\phi)$ and $K_2(\phi)$, as well as the approximated out-of-plane permeability $K_3(\phi) \approx K_2(\phi)/10$, are used to formulate the permeability tensor $\boldsymbol{K}$. Permeability value in thickness direction could not be measured, but its ratio to in-plane values is derived

from [11]. Besides, the K_3 value is assumed to be of low relevance in this linear flow scenario. In Eq. 3, η is the viscosity and $\varphi = 1 - \phi$ the porosity of the stack.

The *incremental flows* $\dot{V}_{\text{flow}}^{(i)}$ across every element surface i (cf. Figure 4) are calculated by means of a midpoint Gaussian integration of the surface integrals

$$\dot{V}_{\text{flow}}^{(i)} = \det\left(\boldsymbol{J_1}\right) \triangle t_{\text{inc}} \left(\frac{\boldsymbol{K}(\phi)}{\eta\,\varphi} \cdot \boldsymbol{B_1}^{\top} \cdot \boldsymbol{J_1}^{-\top} \cdot \boldsymbol{p} \right) \cdot \boldsymbol{n}^{(i)}, \quad \text{with} \quad i = [1, 5]\,, \tag{4}$$

where $\boldsymbol{n}^{(i)}$ provides the current outward normal vector of the current surface. The surface integration is also used to implement the inflow boundary condition at the inlet. Only a one-sided (weak) FSI is used in this work. Hence, deformation directly affects the pressure field, but fluid pressure is not considered in the material deformation.

Model Application

This section is dedicated to several deforming- and infiltration-based scenarios to evaluate the model's response and prediction accuracy. A step-by-step approach is used to verify different model parts, starting with the predicted deformation and reaction forces. First, deep-drawing of a single metal sheet is compared to experimental results. Increasing complexity, a hybrid stack with a homogenized textile interlayer is evaluated in a second step. Here, the three GF layers are combined into one thicker layer. Ultimately, the three GF layers are discretized into individual instances, allowing inter-ply sliding. Moreover, infiltration is introduced to the model to investigate the through-flow and pressure distribution.

Deep drawing of a single metal sheet. A tool setup following the above-outlined segmentation and boundary conditions (cf. Fig. 2 (b)) is combined with a single layer of DC04. Symmetry along the $0\,^\circ$ fiber axis is utilized to reduce the model to a half model (cf. Fig. 2 (c)). The experimental test is conducted at dry conditions and room temperature. The simulation model at this point solely comprises built-in methods of ABAQUS/explicit. A structured triangular mesh with 1380 S3R elements is used, refined in the middle range.

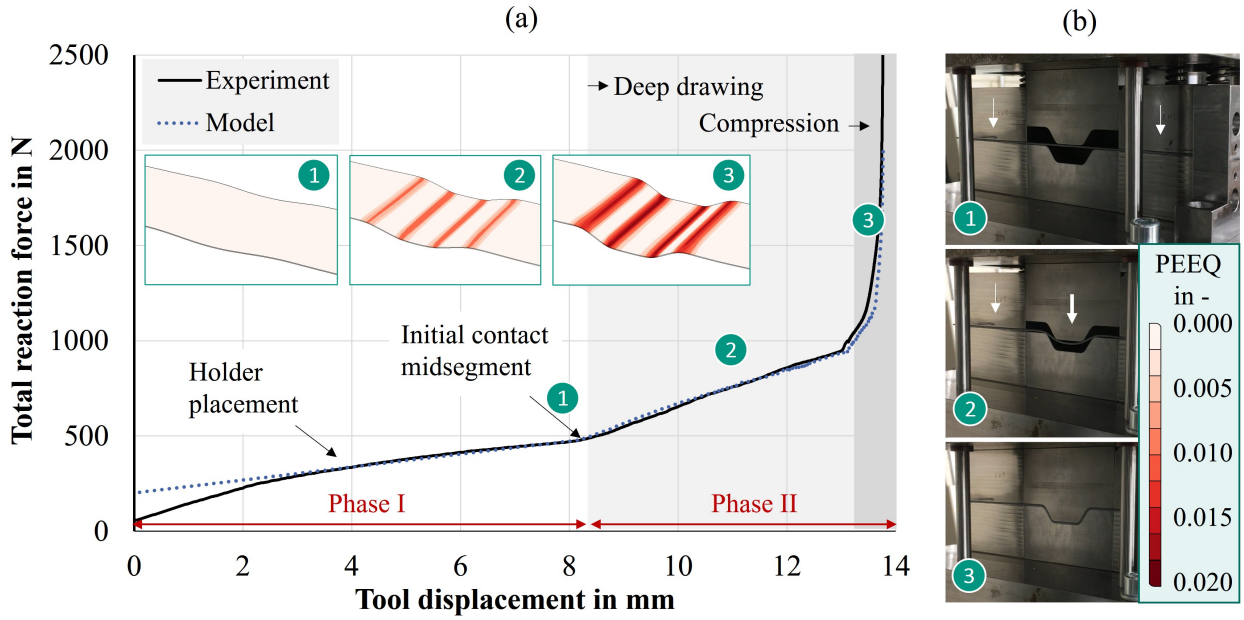

Fig. 6: (a) Comparison of the measured and predicted reaction forces during deep-drawing of a single metal sheet (half model); (b) Images during different stages during experiments. Additionally: Plastic strain (PEEQ) at three distinct points.

Fig. 6 shows the measured and predicted reaction forces during tool phases I (Clamping) and II (Deep drawing), including the wide areal compression towards the end. The springs lead to a relatively constant increase of the total reaction forces within the first phase. After compaction, the second phase (II) is entered, when the midsegment starts to deep-draw the metal sheet into the U-shape. A good agreement is observed for the simulation model. The initial offset in the simulation originates from the load boundary conditions replacing the springs in the model. This confirms the modeling approach and the experimental data published by Trzepiecinski and Lemu [36]. The prediction of the plastic strain in the metal sheet (cf. Fig. 6) reveals that plastic deformation originates from the contact points between metal sheets and tools. Initial plastic deformation is already predicted between points (1) and (2), emphasizing their consideration for modeling metal sheets.

Deep drawing of the dry hybrid stack. A similar experiment is conducted with a dry hybrid stack by adding the second metal layer and the GF interlayers. Regarding the numerical model, the process modeling approach outlined in Fig. 4 (deactivated fluid submodel) is applied. Two configurations are compared on the numerical side – one approach models only one homogenized GF interlayer with tripled thickness. The second configuration contains all three individual GF interlayers, similar to the experiments. Individual contact pairs are assigned at each available interface. Each GF layer consists of 9880 elements, equally divided into continuum shell elements and user elements for compaction modeling.

Fig. 7 provides the obtained curves, including the already in Fig. 6 presented results for the single metal sheet, which only serve as a reference. The total reaction forces of the hybrid stack are consistently higher compared to trials with only one metal sheet.

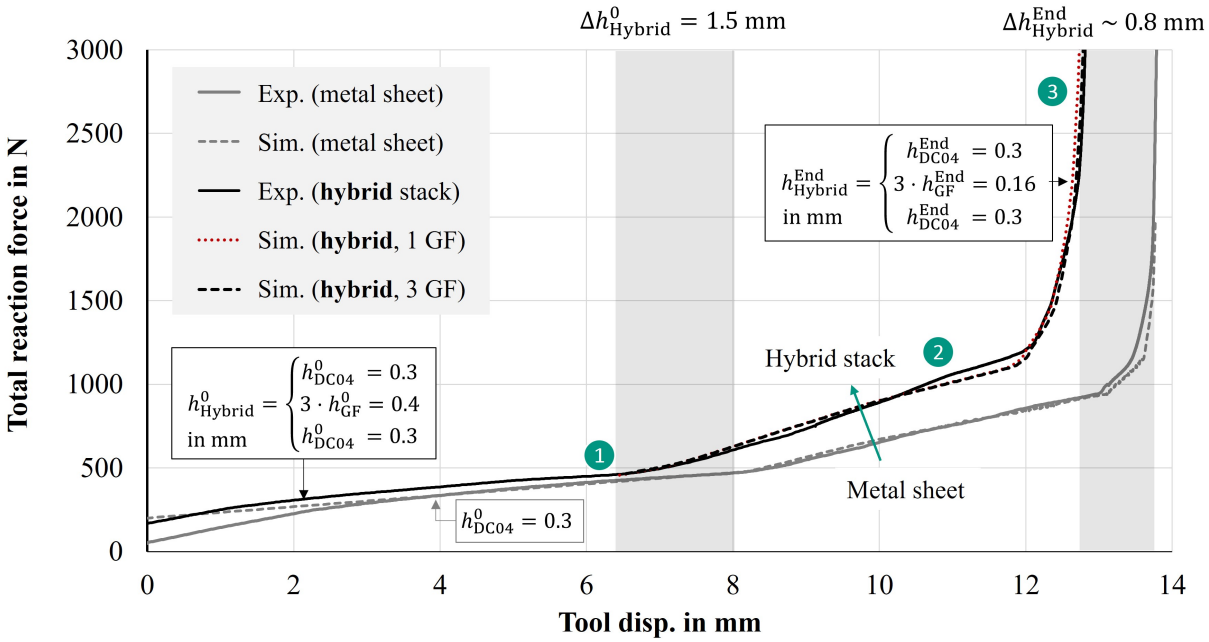

Fig. 7: Comparison of the measured and predicted reaction forces during deep-drawing of the hybrid stack with compactible GF layers (half model). The spatial distribution of the FVC in the GF layers at the distinct points (1)-(3) is shown in Fig. 8.

This result is understandable, as the bending stiffness of the hybrid stack is much higher due to the extra metal sheet and GF layers in between. The undeformed hybrid specimen is $\triangle h^0_{\text{Hybrid}} = 1.5\,\text{mm}$ thicker than the metal layer, which leads to increased compressed springs below the holders. As the stack center region below the midsegment of the specimen remains almost undeformed, the initial contact between midsegment and upper metal sheet is shifted by $\triangle h^0_{\text{Hybrid}} = 1.5\,\text{mm}$. Compaction

of the three GF layers reduces the stack height of the hybrid stack during deep-drawing, the final specimen height difference reduces to $\triangle h^{\text{End}}_{\text{Hybrid}} \approx 0.8\,\text{mm}$ (cf. Fig. 7).

It is observed that both setups, containing either three distinctly modeled GF layers or one homogenized GF layer, match the experimental results quite well. It is concluded that the bending behavior of the hybrid stack is driven by the bending stiffness of the metal sheets and not the GF layers because the increased transverse shear stiffness of the homogenized configuration does not seem to affect the overall result significantly. Hence, computing time can be reduced when the homogenized approach for the GF layers is adopted, yet this also reduces the resolution of the predicted deformation, for example, if one is interested in the differences between the FVCs in the thickness direction in critical regions. Moreover, this is only valid for layers with similar fiber orientation.

The numerical simulation allows investigating and understanding the deformation behavior of the hybrid stack. Fig. 8 illustrated the predicted FVC within the GF interlayer during three time points during mold closure. Initial compaction below the two holder segments leads to FVCs up to $45\,\%$,

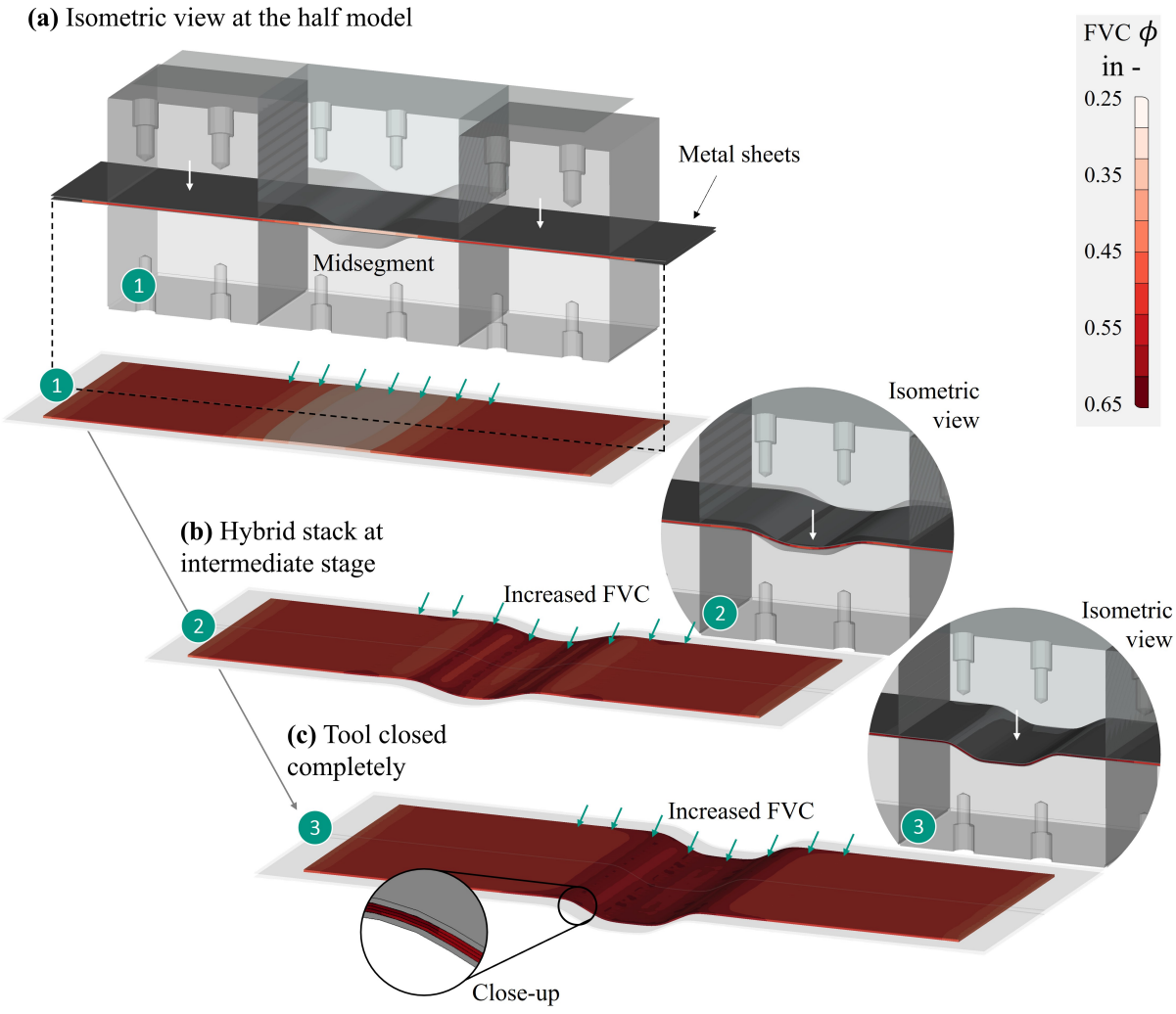

Fig. 8: Stack deformation with local fiber volume content (FVC) for time points (1)-(3) (cf. Fig. 7).

whereas the ply areas below the midsegment remain almost undeformed (cf. Fig. 8 (a)). Moreover, the enlarged metal sheets, required to seal the lateral edges, lead to slightly higher FVCs towards the lateral edges of the hybrid specimens. The metal sheets strongly dominate the bending behavior of the stack. As expected, the highest FVCs during deep-drawing are predicted at the curved edges of the tool (2). The final state is governed by the closed midsegment leading to FVCs around 60 to $65\,\%$ and the slightly lower compaction ($50\,\%$) below the holders.

Simultaneous infiltration. Given the reasonable prediction of the hybrid's stack deformation, infiltration is added to the model. Regarding modeling (cf. Fig. 4), the draping submodel remains identical to the previous section, and inlet and vent boundary conditions are prescribed to the superimposed fluid submodel (cf. Fig. 9 (a)). Recalling Eq. 3 and 4, infiltration is therefore modelled by a porous media flow (Darcy's law) in conjunction with a saturated-based transient expansion of the infiltrated domain. The model is solely solved within ABAQUS/explicit by means of several in-house subroutines [34].

Note: This section is intended to be a first feasibility study of the proposed numerical approach, and not a comprehensive investigation or verification of infiltration.

During *infiltration* and simultaneous draping, the initially linear flow front (cf. Fig. 9 (a.1)) becomes two-dimensional (in-plane), especially towards the midsegment of the tool (cf. Fig. 9 (a.2-4)). The increased FVC at lateral sealing of the hybrid stack (cf. Fig. 8) is responsible for this. Consequently, the predicted pressure distribution along the injected stack is not completely linear, as Fig. 9 (b) shows. This prediction will be considered during the evaluation of the experimentally determined flow rates.

The *pressure distribution* shows that most of the flow resistance originates from the flange areas between the edges, as the pressure gradient increases in these regions. Hence, critical geometrical features need to be optimized concerning deep-drawing and infiltration, and the numerical simulation must capture both topics.

Note that the investigated setup does not require a fully-coupled approach for deformation and infiltration. A sequential approach, combining (1) deep-drawing, (2) infiltration, would also yield similar results. However, this is no longer valid for the ultimately desired HY-LCM process (cf. Fig. 1), where both mechanisms mutually affect one another.

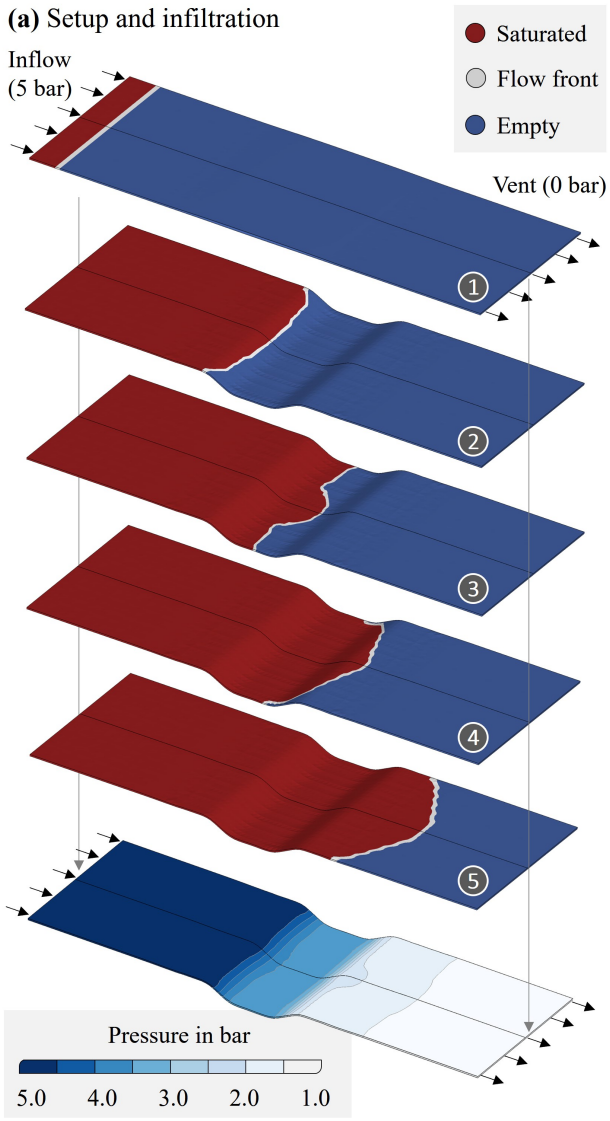

(b) Pressure distribution (fully saturated)

Fig. 9: Simultaneous infiltration of the hybrid stack; (a) Flow front progression; (b) Final pressure distribution for the fully saturated specimen.

Conclusion

A process simulation approach to model combined deep-drawing and infiltration of FMLs is presented and compared with experimental results obtained with a new experiment setup. Ultimately, this work aims to support virtual process development and design of a recently introduced HY-LCM process (cf. Fig. 1), which allows manufacturing of complex-shaped FMLs in a single process step [1, 5–7].

A *new device* (cf. Fig. 2) is used for experimental investigation of hybrid specimens under close-to-process conditions. Results provide vital verification data for the development of the process model. Compaction behavior in thickness direction (cf. Fig. 5) and in-plane permeability values (cf. Fig. 3) of the GF interlayers were characterized using a flat midsegment. Furthermore, dry deep-drawing trials

with a metal sheet and the hybrid stack were conducted, while reaction forces were recorded (cf. Fig. 6 and Fig. 8).

An existing *process model* from WCM simulation is enhanced to capture both metal and textile forming. The model predicts the reaction forces of a dry hybrid stack with compactible GF interlayers (cf. Fig. 8). In this case, the three GF layers between the metal sheets can be homogenized to a single layer, as they share the same fiber orientation. Furthermore, the simulation predicts that the *lateral sealing* of the hybrid stack leads to an inhomogeneous distribution of the FVC perpendicular to the primary fiber orientation. As a consequence, flow progression and pressure distribution become two-dimensional during infiltration (cf. Fig. 9). This information is important for the ongoing evaluation of the injection trials. Although similar results could have been achieved with a decoupled description of deformation and infiltration, the fully-coupled modeling approach will be required when transferring the results to the actual process.

Outlook. Future work at the KIT will draw on the here presented results and further investigate the infiltration behavior. The flow rates at different deformation states need to be analyzed and compared to the numerical predictions of the model. Furthermore, strong FSI requires investigation, especially when applying the process model to the in-situ hybridization process (HY-LCM, cf. Fig 1). Beyond that, heat transfer and curing need to be implemented in the model in order to capture the rapidly changing viscosity during processing. Ultimately, the process model needs to validated with experimental trials on part level, which will be provided by the LUL.

Acknowledgement

The authors would like to thank the German Research Foundation (DGF) for funding the projects HE6154/4-1 and HE 6154/4-2. Moreover, the authors would like to thank the German Federal Ministry of Education and Research (BMBF) for the funding of the project *"HyWet"* (03INT614AC) as part of the *Transatlantic cluster for Lightweighting* (TraCLight), for which some presented numerical methods were developed. This work is also part of the Young Investigator Group (YIG) *"Tailored Composite Materials for Lightweight Vehicles"*, gratefully funded by the Vector Stiftung.

Author Contributions

Christian T. Poppe: Methodology, Software, Validation, Formal analysis, Investigation, Writing - Original Draft, Writing - Review & Editing, Visualization, Supervision; **Henrik O. Werner**: Software, Resources, Writing - Review; **Moritz Kruse**: Conceptualization, Resources, Formal analysis, Validation, Writing - Review; **Hui Chen**: Conceptualization, Resources; **Noomane Ben Khalifa**: Funding acquisition, Project administration; **Frank Henning**: Funding acquisition; **Luise Kärger**: Supervision, Writing - Review

References

[1] T. Mennecart, H. Werner, N. Ben Khalifa, and K. Weidenmann. Developments and Analyses of Alternative Processes for the Manufacturing of Fiber Metal Laminates. In *Proceedings of the ASME 13th International Manufacturing Science and Engineering Conference -2018-*, New York, N.Y., 2018. The American Society of Mechanical Engineers.

[2] S. Krishnakumar. Fiber Metal Laminates — The Synthesis of Metals and Composites. *Materials and Manufacturing Processes*, 9(2):295–354, 1994.

[3] A. Asundi and Alta Y.N. Choi. Fiber metal laminates: An advanced material for future aircraft. *Journal of Materials Processing Technology*, 63(1-3):384–394, 1997.

[4] M. R. Sadeghi, Ali A. A. Jeddi, and S. Shaikhzadeh Najar. Theoretical and experimental analysis of bending rigidity of plain and twill woven fabrics. *Journal of the Textile Institute*, 108(10):1700–1706, 2017.

[5] T. Mennecart, L. Hiegemann, and N.B. Khalifa. Analysis of the forming behaviour of in-situ drawn sandwich sheets. *Procedia Engineering*, 207:890–895, 2017.

[6] H.O. Werner, C.T. Poppe, F. Henning, and L. Kärger. Material Modeling in Forming Simulation of Three-Dimensional Fiber-Metal-Laminates – A Parametric Study. *Procedia Manufacturing*, 47:154–161, 2020.

[7] H.O. Werner, C. Stern, and K. Weidenmann. Location-Dependent Mechanical Properties of In Situ Polymerized Three-Dimensional Fiber-Metal Laminates. *Key Engineering Materials*, 809:231–236, 2019.

[8] R. Arbter, J. M. Beraud, C. Binetruy, and et al. Experimental determination of the permeability of textiles: A benchmark exercise. *Composites Part A: Applied Science and Manufacturing*, 42(9):1157–1168, 2011.

[9] N. Vernet, E. Ruiz, S. Advani, and et al. Experimental determination of the permeability of engineering textiles: Benchmark II. *Composites Part A: Applied Science and Manufacturing*, 61:172–184, 2014.

[10] F. J. Schirmaier, D. Dörr, F. Henning, and L. Kärger. A macroscopic approach to simulate the forming behaviour of stitched unidirectional non-crimp fabrics (UD-NCF). *Composites Part A: Applied Science and Manufacturing*, 102:322–335, 2017.

[11] C. T. Poppe, C. Krauß, F. Albrecht, and L. Kärger. A 3D process simulation model for wet compression moulding. *Composites Part A*, 145:106379, 2021.

[12] A. Willems. *Forming simulations of textile reinforced composite shell structures*. Doctoral thesis, Katholieke Universiteit Leuven, Herverlee, Belgium, 2008.

[13] S. P. Haanappel, R.H.W. ten Thije, U. Sachs, B. Rietman, and R. Akkerman. Formability analyses of uni-directional and textile reinforced thermoplastics. *Composites Part A: Applied Science and Manufacturing*, 56:80–92, 2014.

[14] P. Boisse, N. Naouar, and A. Charmetant. Finite element analysis of composite forming at macroscopic and mesoscopic scale. In Philippe Boisse, editor, *Advances in composites manufacturing and process design*, Woodhead publishing series in composites science and engineering, pages 297–315. Woodhead Publishing, Cambridge, UK, 2015.

[15] P. Boisse, J. Colmars, N. Hamila, N. Naouar, and Q. Steer. Bending and wrinkling of composite fiber preforms and prepregs. a review and new developments in the draping simulations. *Composites Part B: Engineering*, 141:234–249, 2018.

[16] D. Dörr, F.J. Schirmaier, F. Henning, and L. Kärger. A viscoelastic approach for modeling bending behavior in finite element forming simulation of continuously fiber reinforced composites. *Composites Part A: Applied Science and Manufacturing*, 94:113–123, 2017.

[17] D. Dörr, F. Henning, and L. Kärger. Nonlinear hyperviscoelastic modelling of intra-ply deformation behaviour in finite element forming simulation of continuously fibre-reinforced thermoplastics. *Composites Part A: Applied Science and Manufacturing*, 109:585–596, 2018.

[18] P. Boisse, Y. Aimène, A. Dogui, S. Dridi, S. Gatouillat, N. Hamila, M. Aurangzeb Khan, T. Mabrouki, F. Morestin, and E. Vidal-Sallé. Hypoelastic, hyperelastic, discrete and semi-discrete approaches for textile composite reinforcement forming. *International Journal of Material Forming*, 3(2):1229–1240, 2010.

[19] P. Bussetta and N. Correia. Numerical forming of continuous fibre reinforced composite material: A review. *Composites Part A: Applied Science and Manufacturing*, 113:12–31, 2018.

[20] P. Ermanni, C. Di Fratta, and F. Trochu. Molding: Liquid Composite Molding (LCM). In Luigi Nicolais, Assunta Borzacchiello, and Stuart M. Lee, editors, *Encyclopedia of composites*. Wiley online library, [S.l.], 2012.

[21] C.D. Rudd, A.C. Long, K.N. Kendall, C.G.E. Mangin. *Liquid moulding technologies: Resin transfer moulding, structural reaction injection moulding and related processing techniques*. Woodhead, Cambridge, 1997.

[22] P. Celle, S. Drapier, and J.M. Bergheau. Numerical aspects of fluid infusion inside a compressible porous medium undergoing large strains. *Revue européenne de mécanique numérique*, 17(5-6-7):819–827, 2008.

[23] J. Bergstrom. *Mechanics of solid polymers: Theory and computational modeling*. William Andrew is an imprint of Elsevier, Amsterdam, first edition edition, 2015.

[24] A. Bernath, L. Kärger, and F. Henning. Accurate Cure Modeling for Isothermal Processing of Fast Curing Epoxy Resins. *Polymers*, 8(11):390, 2016.

[25] K. M. Pillai, C. L. Tucker, and F. R. Phelan. Numerical simulation of injection/compression liquid composite molding. Part 2: Preform compression. *Composites Part A: Applied Science and Manufacturing*, 32(2):207–220, 2001.

[26] F. Henning, L. Kärger, D. Dörr, F.J. Schirmaier, J. Seuffert, and A. Bernath. Fast processing and continuous simulation of automotive structural composite components. *Composites Science and Technology*, 171:261–279, 2019.

[27] J. Seuffert, P. Rosenberg, L. Kärger, F. Henning, M.H. Kothmann, and G. Deinzer. Experimental and numerical investigations of pressure-controlled resin transfer molding (PC-RTM). *Advanced Manufacturing: Polymer & Composites Science*, 6(3):154–163, 2020.

[28] J. Merotte, P. Simacek, and S.G. Advani. Resin flow analysis with fiber preform deformation in through thickness direction during Compression Resin Transfer Molding. *Composites Part A: Applied Science and Manufacturing*, 41(7):881–887, 2010.

[29] M. V. Bruschke and S. G. Advani. A finite element/control volume approach to mold filling in anisotropic porous media. *Polymer Composites*, 11(6):398–405, 1990.

[30] M. V. Bruschke and S. G. Advani. A numerical approach to model non-isothermal viscous flow through fibrous media with free surfaces. *International Journal for Numerical Methods in Fluids*, 19(7):575–603, 1994.

[31] F. Trochu, E. Ruiz, V. Achim, and S. Soukane. Advanced numerical simulation of liquid composite molding for process analysis and optimization. *Composites Part A: Applied Science and Manufacturing*, 37(6):890–902, 2006.

[32] T.J.R. Hughes, A. Masud, and J. Wan. A stabilized mixed discontinuous Galerkin method for Darcy flow. *Computer Methods in Applied Mechanics and Engineering*, 195(25-28):3347–3381, 2006.

[33] C.T. Poppe, F. Albrecht, C. Krauß, and L. Kärger. A 3D Modelling Approach for Fluid Progression during Process Simulation of Wet Compression Moulding – Motivation and Approach. *Procedia Manufacturing*, 47:85–92, 2020. 23rd International Conference on Material Forming.

[34] C.T. Poppe. *Process simulation of wet compression moulding for continuous fibre-reinforced polymers*. Doctoral thesis, Karlsruher Institut für Technologie (KIT), 2021.

[35] C. Poppe, D. Dörr, F. Henning, and L. Kärger. A 2D modeling approach for fluid propagation during FE-forming simulation of continuously reinforced composites in wet compression moulding. AIP Conference Proceedings, page 020022. Author(s), 2018.

[36] T. Trzepiecinski and H. Lemu. Effect of Computational Parameters on Springback Prediction by Numerical Simulation. *Metals*, 7(9):380, 2017.

[37] P. Potluri and T. V. Sagar. Compaction modelling of textile preforms for composite structures. *Composite Structures*, 86(1):177–185, 2008.

[38] J.P.-H. Belnoue, M.A. Valverde, M. Onoufriou, X. Sun, D.S. Ivanov, and S.R. Hallett. On the physical relevance of power law-based equations to describe the compaction behaviour of resin infused fibrous materials. *International Journal of Mechanical Sciences*, 199:106425, 2021.